Research Paper

Tumor microenvironment-activated single-atom platinum nanozyme with H_2O_2 self-supplement and O_2-evolving for tumor-specific cascade catalysis chemodynamic and chemoradiotherapy

Qiqi Xu[1,2*], Yuetong Zhang[1,2*], Zulu Yang[1,2], Guohui Jiang[6], Mingzhu Lv[1,2], Huan Wang[1,2], Chenghui Liu[1,2], Jiani Xie[4], Chengyan Wang[3], Kun Guo[5], Zhanjun Gu[3], Yuan Yong[1, 2✉]

1. Key Laboratory of Pollution Control Chemistry and Environmental Functional Materials for Qinghai-Tibet Plateau of the National Ethnic Affairs Commission, School of Chemistry and Environment, Southwest Minzu University, Chengdu 610041, China.
2. Key Laboratory of General Chemistry of the National Ethnic Affairs Commission, School of Chemistry and Environment, Southwest Minzu University, Chengdu 610041, China.
3. CAS Key Laboratory for Biomedical Effects of Nanomaterials and Nanosafety, Institute of High Energy Physics, Chinese Academy of Sciences, Beijing100040, China.
4. College of Pharmacy and Biological Engineering, Chengdu University, Chengdu, 610106, China.
5. College of Pharmacy, Southwest Minzu University, Chengdu 610041, China.
6. Department of Neurology, Affiliated Hospital of North Sichuan Medical College, Nanchong 637000, China.

*These authors contributed equally.

✉ Corresponding author: Yuan Yong, E-mail: yongy1816@163.com

Abstract

Nanozyme-based tumor collaborative catalytic therapy has attracted a great deal of attention in recent years. However, their cooperative outcome remains a great challenge due to the unique characteristics of tumor microenvironment (TME), such as insufficient endogenous hydrogen peroxide (H_2O_2) level, hypoxia, and overexpressed intracellular glutathione (GSH).

Methods: Herein, a TME-activated atomic-level engineered PtN_4C single-atom nanozyme (PtN_4C-SAzyme) is fabricated to induce the "butterfly effect" of reactive oxygen species (ROS) through facilitating intracellular H_2O_2 cycle accumulation and GSH deprivation as well as X-ray deposition for ROS-involving CDT and O_2-dependent chemoradiotherapy.

Results: In the paradigm, the SAzyme could boost substantial ·OH generation by their admirable peroxidase-like activity as well as X-ray deposition capacity. Simultaneously, O_2 self-sufficiency, GSH elimination and elevated Pt^{2+} release can be achieved through the self-cyclic valence alteration of Pt (IV) and Pt (II) for alleviating tumor hypoxia, overwhelming the anti-oxidation defense effect and overcoming drug-resistance. More importantly, the PtN_4C-SAzyme could also convert O_2^- into H_2O_2 by their superior superoxide dismutase-like activity and achieve the sustainable replenishment of endogenous H_2O_2, and H_2O_2 can further react with the PtN_4C-SAzyme for realizing the cyclic accumulation of ·OH and O_2 at tumor site, thereby generating a "key" to unlock the multi enzymes-like properties of SAzymes for tumor-specific self-reinforcing CDT and chemoradiotherapy.

Conclusions: This work not only provides a promising TME-activated SAzyme-based paradigm with H_2O_2 self-supplement and O_2-evolving capacity for intensive CDT and chemoradiotherapy but also opens new horizons for the construction and tumor catalytic therapy of other SAzymes.

Key words: Single-atom nanozyme, tumor microenvironment-activated, enzyme-like activity, tumor catalytic therapy, chemodynamic and chemoradiotherapy

Introduction

Chemodynamic therapy (CDT), which takes advantage of iron-mediated Fenton reaction or Cu^{2+}-/Mn^{2+}-mediated Fenton-like reaction to convert less reactive H_2O_2 into highly toxic ·OH for inducing

cell apoptosis and necrosis [1-4], has attracted widespread attention in recent years due to its high selectivity and logicality as well as activation of endogenous stimuli [5-9]. To date, despite tremendous efforts have been achieved in triggering tumor cells apoptosis by the endogenous H_2O_2-dependent Fenton reaction in CDT [10-14], their therapeutic effectiveness remains a great challenge due to the tumor microenvironment (TME) characterized by insufficient endogenous hydrogen peroxide (H_2O_2, $50-100\times10^{-6}$ M) [6,15-17], overexpressed glutathione (GSH) [18-24] as well as hypoxia microenvironment [25-32]. Therefore, to potentially enhance their antitumor efficiency, several H_2O_2-supplementing strategies have been applied to convey exogenous H_2O_2 or trigger endogenous H_2O_2 generation in the tumor site [16, 33-37]. Unfortunately, these methods still suffer from the drawbacks of the premature release of H_2O_2 and tumor hypoxia as well as sophisticated genetic engineering. Therefore, how to explore straightforward and evolutionary paradigm capable of H_2O_2-supplementing *in situ*, overcoming tumor hypoxia and constantly depleting GSH is urgently required but challenging for enhanced CDT, thus greatly breaking through therapeutic resistance and eradicating the tumor completely.

As we all known, hypoxia, as another characteristic feature of TME, is a barrier to tumor therapy and responsible for tumor migration, invasion, metastasis, and resistance [38-41]. On account of this, chemoradiotherapy is usually utilized as a combination therapy for attenuating tumor hypoxia and lessening the chance of tumor recurrence clinically [42-44]. So far, the reprogramming method of tumor hypoxia in chemoradiotherapy includes not only internal unique pathological stimuli by utilizing some smart nanomedicines delivering O_2-triggering agents [45-49], but also hypoxic cell sensitization by the introduction of high-Z radiosensitizer or chemotherapeutics [50-53]. Nevertheless, these relevant strategies for overcoming hypoxia commonly involve poor therapeutic effect or serious side effects on normal tissue. Therefore, in order to overcome tumor hypoxia and endogenous H_2O_2 deficiency simultaneously, it is essential and highly desirable to develop a versatile and TME-initiated nanomedicine, which has with the capacity of irradiation deposition, substantial drug release, persistent O_2 and H_2O_2 cyclic replenishment at tumor site, thereby greatly improving the efficiency of CDT and chemoradiotherapy for synergistically eradicate tumor.

Nanozymes, with intrinsic enzyme-like characteristics, have sparked increasing interest in the biomedical field due to their tunable catalytic activity, high stability, and low cost [17, 54-61]. Among the various reported paradigms, single-atom nanozymes (SAzymes) as a special kind of nanozymes with maximum atomic utilization efficiency, high density active sites and superior multienzyme-like activity as well as selectivity has emerged as prospective platform for TME-activated nanozyme-based tumor-specific catalytic therapy [62-67]. By utilizing these unique superiorities, herein, a novel and TME-activated PtN_4C-SAzyme was proposed to achieve continuous H_2O_2 self-replenishment, O_2-evolving and GSH elimination as well as Pt^{2+} release for intensive synergistic CDT and chemoradiotherapy. The resultant system possesses several attractive advantages: i) The SAzyme could boost substantial $\cdot OH$ and O_2 generation by their admirable peroxidase- and catalase-like activity as well as X-ray deposition capacity, which facilitated to oxygenate TME for intensive CDT and O_2-dependent chemoradiotherapy; ii) Meanwhile, the self-cyclic valence alteration of Pt (IV) and Pt (II) endowed continuous depletion of intracellular overexpressed GSH and substantial Pt^{2+} release to overwhelm the anti-oxidation defense effect for enhanced tumor-specific therapy, ultimately; iii) More importantly, the PtN_4C-SAzyme could also convert O_2^{-} into H_2O_2 and achieve the sustainable replenishment of H_2O_2 *in situ* of tumor, and H_2O_2 can further react with the PtN_4C-SAzyme for realizing the cyclic accumulation of $\cdot OH$ and O_2, thereby in turn generating a "key" to unlock the multiple enzyme-like properties of SAzymes for tumor-specific CDT and chemoradiotherapy. Taken together, our work provides a new TME-activated SAzyme-based high-performance anti-tumor paradigm with the ability to self-supplement H_2O_2 and boost O_2-evolving as well as deplete intracellular GSH for tumor-specific cascade catalytic CDT and chemoradiothearpy.

Results and discussion

To substantiate our protocol, the PtN_4C-SAzyme was successfully synthesized according to a reported strategy with a slight modification (**Scheme 1**) [68, 69]. Representative scanning electron microscopy (SEM) indicated that the PtN_4C-SAzyme exhibited uniform size and spheroid morphology (**Figure 1A**). Corresponding dynamic light scattering (DLS) measurement confirmed that PtN_4C-SAzyme possessed admirable dispersion with an average hydrodynamic diameter of about 110 nm (**Figure 1A**), which was facilitated to uptake and penetrate nanomedicines at tumor site due to the enhanced permeability and retention (EPR) effect [70]. Furthermore, the element mappings and energy-dispersive spectroscopy (EDS) spectrum

showed the Pt, N and C atoms were homogeneously distributed over the entire architecture of PtN$_4$C-SAzyme (**Figure 1B**), and Pt and N content in PtN$_4$C-SAzyme was quantified to be 2.34 and 39.92 wt % respectively (**Figure 1C**). Consistently, X-ray diffraction (XRD) pattern of PtN$_4$C-SAzyme disclosed no observable Pt nanoparticles and/or nanoclusters or characteristic crystal peaks, thereby excluding the formation of Pt-based crystalline phases and illustrating the successful formation of PtN$_4$C-SAzyme (**Figure S1**). In addition, Fourier transform infrared spectroscopy (FT-IR) spectra (**Figure S2**), UV/vis absorption spectra (**Figure S3**) and ζ potentials (**Figure S4**) also demonstrated the successful preparation of PtN$_4$C-SAzyme. Moreover, the existence of Pt, N, C elements and Pt-N interaction was further substantiated by X-ray photoelectron spectroscopy (XPS) analysis (**Figure 1D**). Given the importance of metal valence state in tumor catalytic therapy, the high-resolution Pt 4f XPS spectrum was further identified. As shown in **Figure 1E**, Pt-Pt bonds located at 71.2 eV and 74.5 eV was absence, and the deconvolution of XPS spectrum of PtN$_4$C-SAzyme in Pt 4f region showed two characteristic peaks located at 78.5 eV and the peaks at 75.4 eV, respectively, owing to the coexistence of Pt^{4+} and Pt^{2+} [71], which was consistent with XRD result and indicated the successful generation of Pt-N$_x$ sites in three-dimensional skeleton. It is reported that low metal valence state will facilitate the decomposition of H$_2$O$_2$ to ·OH generation under acidic conditions, while the high valence state will promote the generation of O$_2$ by the oxidation of H$_2$O$_2$ [7,17]. Therefore, because of the coexistence of their mixed valence state, PtN$_4$C-SAzyme is greatly anticipated to be a nanozyme with superior peroxidase-like and catalase-like activity for tumor-specific catalytic therapy.
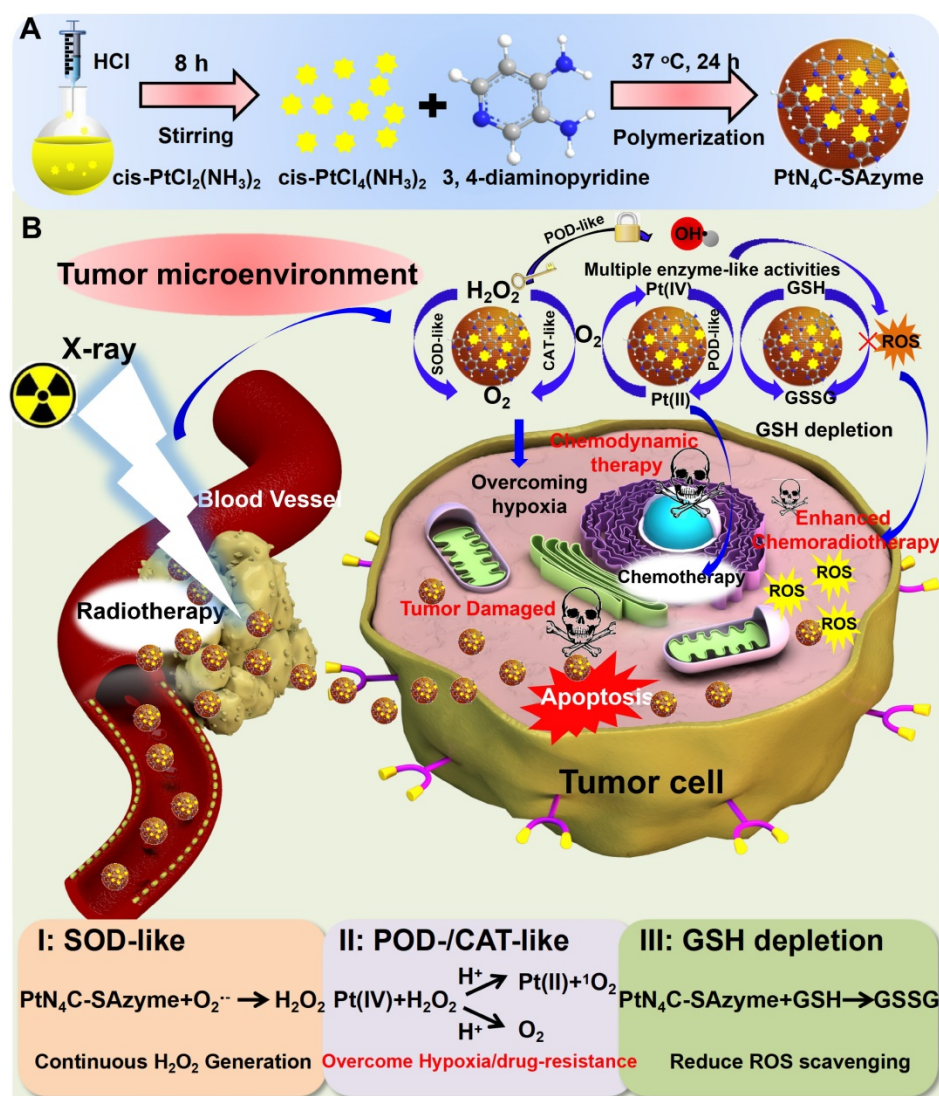
Scheme 1. Schematic illustration of (A) the preparation process of PtN$_4$C-SAzyme and (B) its cascaded catalytic reaction in tumor microenvironment for tumor synergistic enhanced CDT and chemoradiotherapy.
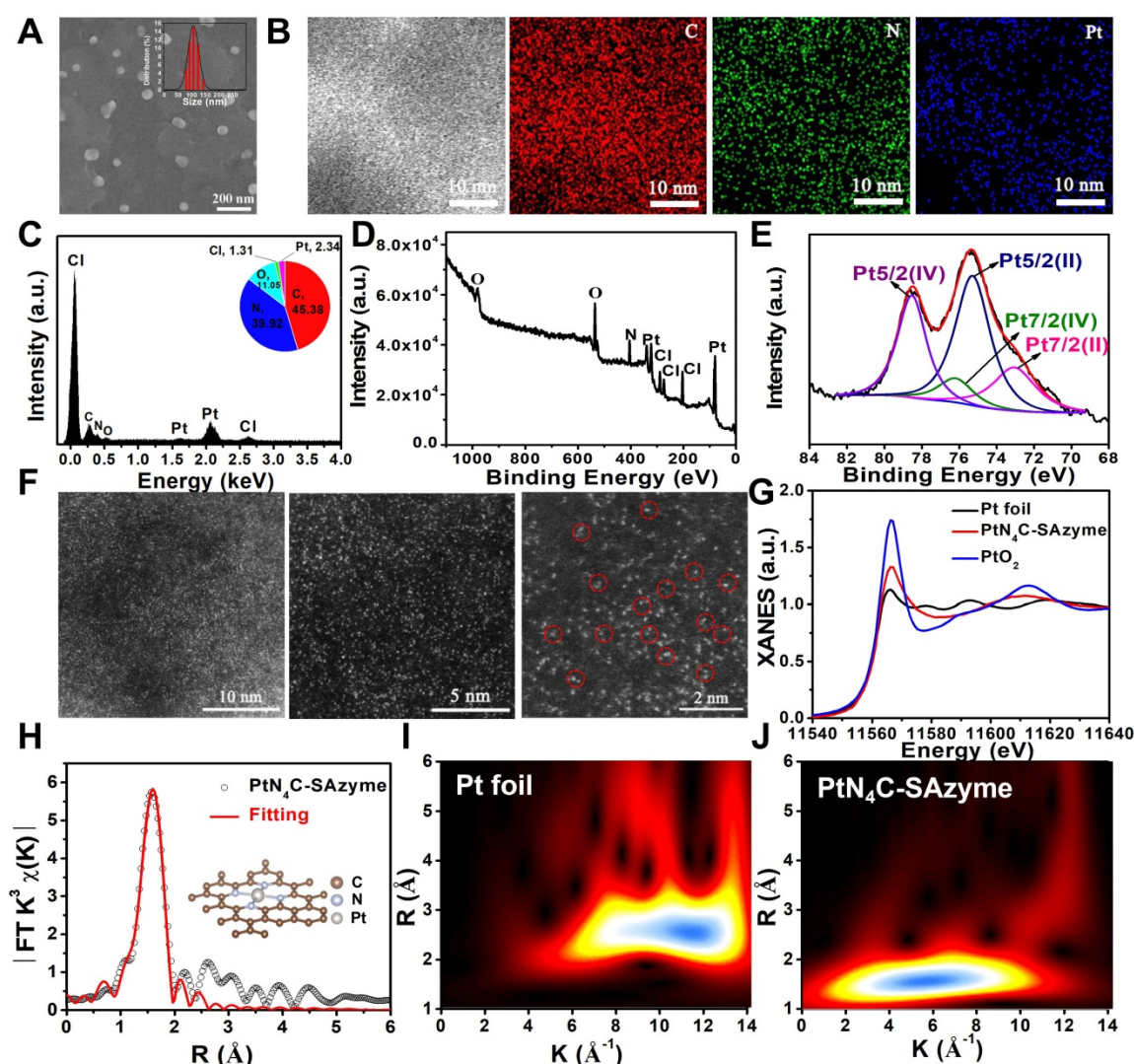
Figure 1. Structural characterizations and atomic structural analysis of PtN₄C-SAzyme. SEM image (A) and the corresponding element mapping (B) of PtN₄C-SAzyme; (C) EDS spectra recorded from the whole area of PtN₄C-SAzyme. XPS spectrum of PtN₄C-SAzyme (D) and high-resolution Pt4f of PtN₄C-SAzyme (E). (F) Aberration-corrected HAADF-STEM image of PtN₄C-SAzyme with different magnification. (G) XANES spectra of Pt foil and PtN₄C-SAzyme. (H) Fourier-transformed magnitudes of the experimental Pt K-edge EXAFS signals of PtN₄C-SAzyme. Wavelet transform (WT) for the k³-weighted EXAFS spectra of (I) Pt foil and (J) PtN₄C-SAzyme.

To verify whether the isolated Pt atoms are atomically dispersed in PtN₄C-SAzyme, aberration-corrected high-angle annular dark-field scanning transmission electron microscopy (HAADF-STEM) characterizations were employed and bright dots highlighted by red circles were recognized to be Pt single atoms in the PtN₄C-SAzyme (**Figure 1F**), directly visually and intuitively demonstrating the existence of isolated Pt atoms. To further validate the local structure and coordination environment of the PtN₄C-SAzyme at an atomic level, synchrotron radiation-based X-ray absorption near-edge structure (XANES) and extended X-ray absorption fine structure spectroscopy (EXAFS) measurements were carried out at Pt K-edge. The near-edge absorption energy position of PtN₄C-SAzyme was located between that of reference samples Pt foil and PtO₂ (**Figure 1G**), indicating that the atomically dispersed

Pt species carried a positive charge between Pt^0 and Pt^{4+}, in accordance with XPS Pt4f spectrum mentioned above. Moreover, Fourier-transformed k³-weighted extended XAFS (FT-EXAFS) spectrum of PtN₄C-SAzyme at Pt K-edge presented a main peak at 1.59 Å, which was drastically different from Pt-Pt bond (2.6 Å) (**Figure 1H**) [72-76], further strongly excluding the existence of Pt-based crystal and confirming the formation of atomically dispersed Pt-Nₓ sites structures in PtN₄C-SAzyme. Furthermore, wavelet transform (WT) of the k³-weighted EXAFS spectra were also obtained in **Figure 1I&J**. As displayed in the contour plot of standard Pt foil, the maximum intensities at ~11.8 was contributed to Pt-Pt bonding. However, an intensity maximum of ~6.1 Å in the PtN₄C-SAzyme is accordant to the Pt-N bonding. Meanwhile, the corresponding EXAFS fitting parameters were listed in **Table S1**. The

obtained surrounding coordination atom (N) of Pt in the PtN$_4$C-SAzyme was about 4 and the bond length between Pt and N atoms was 2.01. Therefore, all these results indicated the Pt in the PtN$_4$C-SAzyme was atomically dispersion.

Subsequently, the mixed valence state of PtN$_4$C-SAzyme inspired us to investigate its multiple enzyme-like catalytic functions for biocatalytic cascade reactions, which plays an important role in the metabolic processes and cancer therapy (**Figure 2A**). In the first place, the ·OH-generating peroxidase-like activity of PtN$_4$C-SAzyme was evaluated by the catalytic oxidation of 3, 3′, 5, 5′-tetramethylbenzidine (TMB) to form the blue-colored oxidized TMB (oxTMB). As depicted in **Figure 2B**, in the presence of PtN$_4$C-SAzyme and H$_2$O$_2$, TMB could be effectively oxidized and showed an obvious absorbance increase at the characteristic peak of 652 nm, whereas with PtN$_4$C-SAzyme or H$_2$O$_2$ alone, the characteristic absorption of oxTMB disappeared, indicating no oxidation reaction was occurred and uncovering the superior peroxidase-like activity of PtN$_4$C-SAzyme. Moreover, the ·OH generation capacity by PtN$_4$C-SAzyme was further monitored through the degradation of methylene blue (MB) (**Figure 2C**). After incubation with PtN$_4$C-SAzyme with H$_2$O$_2$, the MB content significantly decreased by 83.0 %, while no obvious change was observed in PtN$_4$C-SAzyme or H$_2$O$_2$ alone, indicating the effective ·OH generation was driven by the PtN$_4$C-SAzyme-mediated Fenton-like reaction. Meanwhile, we also confirmed the existence of the active intermediate ·OH generation during the catalytic processes by electron spin resonance (ESR) analysis. As described in **Figure 2D,** the signal of DMPO/·OH significantly increased in the presence of PtN$_4$C-SAzyme. And once adding the ·OH scavenger of isopropanol, the absorbance signal of SAzymes markedly declined, further substantiating that ·OH participated in the catalytic processes (**Figure S5**). Furthermore, to elucidate the peroxidase-like catalytic mechanism of PtN$_4$C-SAzyme, the H$_2$O$_2$ decomposition efficiency was determined in the catalytic reaction. The result showed that the concentration of H$_2$O$_2$ significantly decreased once in the presence of PtN$_4$C-SAzyme (**Figure S6**), manifesting that PtN$_4$C-SAzyme with high peroxidase-like catalytic activities had the great potential to decompose H$_2$O$_2$ and generate ·OH. Apart from these, some factor-dependent behaviors like concentration, H$_2$O$_2$, temperature, and pH were also investigated (**Figure S7**). And the catalytic kinetics of PtN$_4$C-SAzyme exhibited a typical Michaelis-Menten kinetics for H$_2$O$_2$ and TMB substrates under the optimal pH and temperature, respectively (**Figure S8-9**). Subseq-

uently, to investigate the PtN$_4$C-SAzyme possessing favorable catalase-like activity, we measured H$_2$O$_2$-triggered O$_2$-evolving in PtN$_4$C-SAzyme by a dissolved oxygen meter, which is crucial for chemoradiotherapy of hypoxia tumor. As expected, the PtN$_4$C-SAzyme exhibited an obvious catalase-like activity in the presence of H$_2$O$_2$ (**Figure 2E&S10**). Although the content of dissolved oxygen (DO) decreased with the decrease of pH value, there was still much higher than that of SAzymes or H$_2$O$_2$ alone at pH 5.0 (**Figure 2F&S11**), implying that the PtN$_4$C-SAzyme could trigger the decomposition of H$_2$O$_2$ to produce O$_2$ under tumor acidic microenvironment and facilitate to alleviate tumor hypoxia. In addition, the catalase-like activity of PtN$_4$C-SAzyme also exhibited samples and H$_2$O$_2$ concentration-dependent manner (**Figure 2G&H**). According to the above results, we could conclude that PtN$_4$C-SAzyme had great promise for tumor CDT and chemoradiotherapy catalytic therapy by their intrinsic H$_2$O$_2$-responsive peroxidase- and catalase-like activities.

As we all known, although the TME is characterized by a low pH value, hypoxia, overexpressed GSH and H$_2$O$_2$ compared with normal physiological condition, the level of inherently endogenous H$_2$O$_2$ ($50-100 \times 10^{-6}$ M) is insufficient to generate substantial ·OH and O$_2$ for achieving tumor satisfactory CDT and chemoradiotherapy therapeutic effect. Therefore, we anticipate our PtN$_4$C-SAzyme possesses superoxide dismutase activity for promoting superoxide anions (O$_2^{\cdot-}$) transformation into H$_2$O$_2$ by disproportionation catalysis, thereby realizing continuous H$_2$O$_2$-supplement for potentiating their CDT and chemoradiotherapy. Unexpectedly, apart from the peroxidase- and catalase-like activities, PtN$_4$C-SAzyme also exhibited the capacity of transforming O$_2^{\cdot-}$ generated from chemoradiotherapy into H$_2$O$_2$ measured by the classic nitroblue tetrazolium (NBT) chromogenic method, achieving the cyclic accumulation of H$_2$O$_2$ at tumor site and subsequently decomposition into ·OH and O$_2$. As displayed in **Figure 2I**, O$_2^{\cdot-}$ in the positive control was generated by irradiation riboflavin and Lmethionine with UV, which could decrease NBT to a water-soluble formazan dye with a strong UV-vis absorbance signal at the characteristic peak of 560 nm. Once PtN$_4$C-SAzyme was added, the absorbance signal decreased significantly. Moreover, the disproportionation of PtN$_4$C-SAzyme to O$_2^{\cdot-}$ also exhibited concentration and pH-dependent (**Figure 2J-K and S12**). With the increase of the SAzyme concentration, the disproportionation of PtN$_4$C-SAzyme to O$_2^{\cdot-}$ was further increased (**Figure 2J**). Notably, PtN$_4$C-SAzyme exhibited better

enzyme-like activity at lower pH conditions (**Figure 2K**), which facilitates the generation of hydrogen peroxide in the acidic tumor microenvironment to enhance tumor therapy. Importantly, as a proof-of-concept, we also adopted KSCN to block Pt sites to confirm the active sites (**Figure 2L**). When in the presence of KSCN, the activity of SAzymes significantly decreased due to the chelation between single Pt atom and SCN-, indirectly revealing Pt-Nx sites act as their active sites. Therefore, all these results indicated that the PtN_4C-SAzyme could act as three-enzymatic co-expression systems for achieving continuous H_2O_2 self-supplement and cyclic accumulation of substantial ·OH and O_2 under TME, so as to greatly boost therapeutic outcome for CDT and chemoradiotherapy of hypoxia tumor.

To shed light on the origin of the multiple enzyme-like activities of PtN_4C-SAzyme, plausible reaction mechanisms and reaction pathways as well as the free energy profiles of the confined Pt site are put forward by density functional theory (DFT) calculation. EXAFS fitting was firstly performed to support the quantitative structural configuration of Pt in the PtN_4C-SAzyme sample with a coordination number of 4.0 (**Table S1**). Therefore, an optimized structure model of Pt-Nx active site embedded in the PtN_4C-SAzyme matrix was established according to experimental characterization, accompany with a

Pt-O bond length of 1.961 and 1.241 Å respectively after adsorption O and O_2 on the PtN_4C-SAzyme (**Figure 3A&B**). As revealed in **Figure 3C**, the geometrically optimized H_2O_2 molecule is initially adsorbed on the top of the Pt active centers (Pt-Nx) of PtN_4C-SAzyme (i), resulting in the adsorbed intermediates (ii) formation with a moderate adsorption energy (H_2O_2*) of 0.29 eV. The activated H_2O_2 molecule is subsequently cleaved to 2OH* (iii) by the single Pt sites ($Pt^{\delta+}$) via a homogeneous pathway (1.005 eV) rather than heterogeneous manner (1.423 eV) (**Figure S13**). Subsequently, the intermediates of a reactive hydroxyl radical (·OH) and a hydroxyl group (OH*) were generated by a hydroxyl group desorption from the single Pt site (iv), accompanying with energy barrier of 0.42 eV, which is easily surmountable at room temperature. Finally, desorption of a ·OH enables the overall regeneration of the SAzymes surface for activating another H_2O_2 molecule to generate ·OH in the next cycle, resulting in a substantial reduction of the total Gibbs free energy and achieving their superior peroxidase-like activity (-0.65 eV) (**Figure S14**). In addition, to further gain insights into the catalase-like activity of PtN_4C-SAzyme toward H_2O_2 oxidation, two possible reaction pathways were put forward by DFT calculation (**Figure S15**). The results indicated that reaction energy barrier for the homolytic pathway of
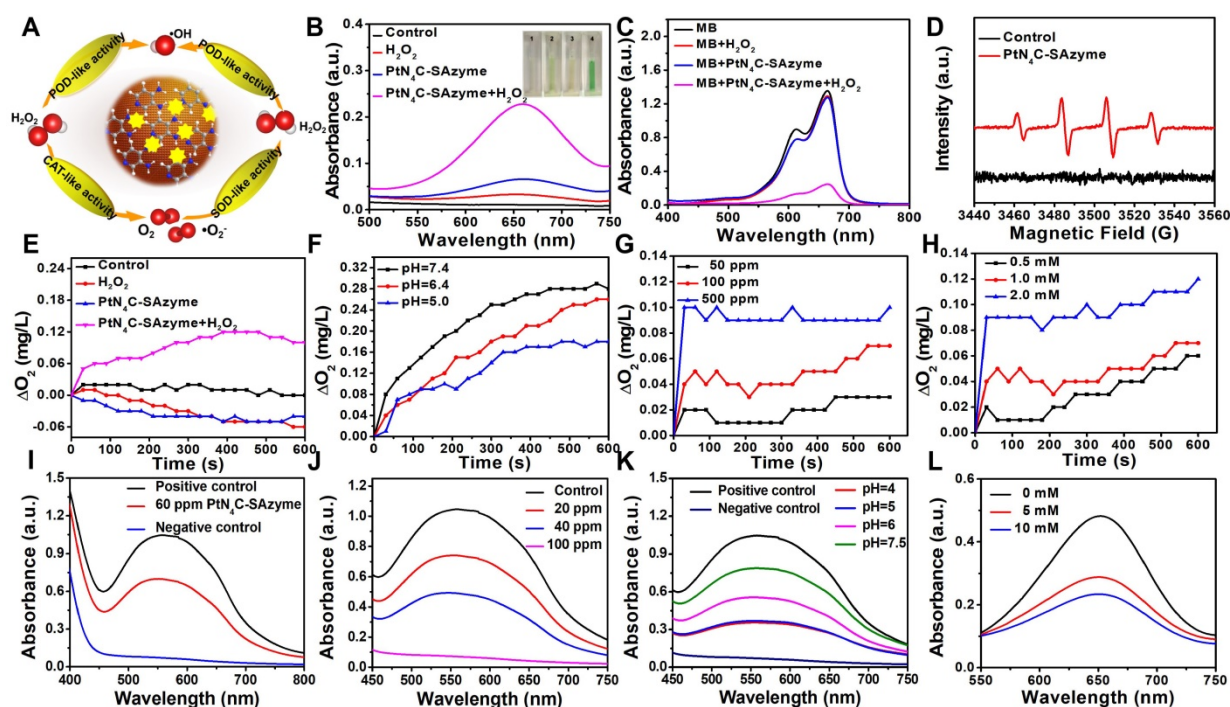

Figure 2. Multiple enzyme-like activities of PtN_4C-SAzyme for tumor microenvironment regulation. (A) Schematic presentation of superoxide dismutase-like, peroxidase-like and catalase-like activities of PtN_4C-SAzyme; (B) Peroxidase-like activities of PtN_4C-SAzyme; (C) The degradation of MB in different solutions by the PtN_4C-SAzyme mediated Fenton-like reaction. (D) EPR spectra for the detection of ·OH from H_2O_2 and PtN_4C-SAzyme+H_2O_2. (E) O_2 generation in different systems in the absence or presence of PtN_4C-SAzyme. (F-H) The catalase-like activity of the PtN_4C-SAzyme is dependent on pH, samples and H_2O_2 concentration. (I) Superoxide dismutase-like of PtN_4C-SAzyme. (J) Catalytic conversion of superoxide radicals by different concentration of PtN_4C-SAzyme. (K) UV-visible absorption of oxidized NBT in different conditions. (L) UV-vis spectra of the peroxidase-like activity of PtN_4C-SAzyme with and without KSCN.

H_2O_2* to $2OH*$ (1.005 eV) was lower than that for the heterolytic pathway of H_2O_2* to $O* + H_2O*$ (1.423 eV), suggesting the homolytic pathway was more kinetically favorable for H_2O_2* dissociation and O_2 generation. Therefore, we adopted the homolytic pathway as a dominant pathway to investigate the reaction mechanism for the enhanced catalase-like activity of PtN_4C-SAzyme. **Figure 3D** showed that the H_2O_2 molecule could be easily adsorbed on the confined Pt site (i) for forming an $Pt-H_2O_2*$ intermediate (ii) and releasing two $OH*$ molecule (iii), followed by the dissociation for generating $O*$ and H_2O molecule (iv) by disproportionation pathway with an energy barrier of -0.38 eV and releasing one H_2O molecule (v) subsequently. Finally, the $O*$ species of the Pt-O was active for the adsorption of another $O*$ via the formation of an O_2 molecule with an energy barrier of -3.87 eV. Therefore, the DFT calculations unambiguously identified that the $Pt-N_x$ centers could play an important role in the adsorption and activation of H_2O_2, which were in agreement with the origin of generating ·OH and O_2 by their superior peroxidase- and catalase-like activity.

Interestingly, apart from their multi-enzyme cascade biocatalytic activity for TME regulation and tumor CDT, we uncovered that the PtN_4C-SAzyme also possessed favorable X-ray-triggered radiosensitization behavior and endogenous GSH-activated Pt^{2+}

release capacity to boost their chemoradiotherapy effciency. In the first place, both 7'-Dichloro-fluorescent yellow diacetate (DCFH-DA) and 5, 5-dimethyl-1-pyrroline N-oxide (DMPO) were employed as probes to monitor the generation of ROS in different systems. As depicted in **Figure 4A&B,** negligible fluorescence or characteristic signals were detected in the group of phosphate buffer, SAzyme solution or X-ray alone. However, the fluorescence intensity and characteristic signals of the PtN_4C-SAzyme solution were significantly increased once in the presence of X-ray. This might be attributed to abundant Pt active sites and strong surface charge density in the surface of PtN_4C-SAzyme for sufficient ROS generation by enhancing X-ray deposition to produce H_2O^+ and H_2O* as well as ·OH in the successive physico-chemical and chemical stages. Moreover, the deprivation of GSH by our SAzymes via the redox reaction was studied, which was facilitated to generate large amounts of ROS for killing the tumor. As displayed in **Figure 4C**, obviously decrease of GSH was induced after incubation with PtN_4C-SAzyme, in comparison with that of N-doped carbon support (NCs). And the consumption of GSH by PtN_4C-SAzyme also exhibited concentration- and time-dependent behaviors (**Figure 4D&S16**), which demonstrated that PtN_4C-SAzyme could effectively promote GSH

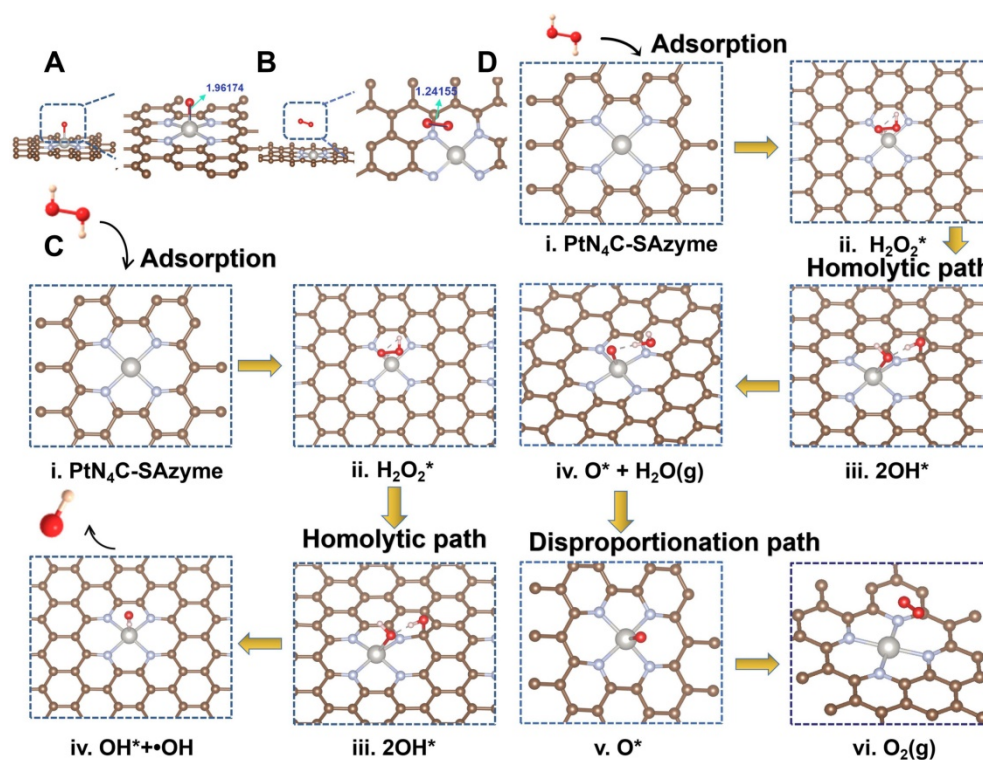**Figure 3. Density functional theory (DFT) calculations of PtN₄C-SAzyme.** Optimized structures of O (A) and O₂ (B) species adsorbed on the surface of PtN₄C-SAzyme, respectively. Interatomic distances are indicated in Å. Proposed catalytic mechanism schematics of peroxidase-like (C) and catalase-like (D) activities of PtN₄C-SAzyme. The dark grey, light grey, gold, red and pink balls represent the Pt, N, C, O and H atoms, respectively.

depletion through redox reaction. Meanwhile, we were surprised to find that the PtN$_4$C-SAzyme could trigger Pt^{2+} release while eliminating GSH (**Figure 4E**), which not only could be used for chemotherapy effect and facilitate to overcome tumor drug-resistance, but also could be again converted to Pt^{4+} by the valence state variation of Pt, endowing the continuous deprivation of GSH. Therefore, a possible enhanced cytotoxicity mechanism of PtN$_4$C-SAzyme may be described as follows (**Figure 4F**). The overexpression of GSH in the tumor can directly diminish the amount of ROS generation and thereby attenuate the cytotoxicity of cancer cells. Hearteningly, we found that the PtN$_4$C-SAzyme can drastically enhance ROS levels through producing Compton and Auger electrons induced by PtN$_4$C-SAzyme with the surrounding water or oxygen molecules and consuming GSH as well as

promoting cytotoxic Pt^{2+} release by the redox reaction, thus effectively enhancing collaborative anti-tumor effect. Furthermore, the ROS-evolving properties of PtN$_4$C-SAzyme under X-ray irradiation in cancer cells were also evaluated by utilizing the 2', 7-dichloro-dihydrofluorescein diacetate (DCFH-DA) probe. Indeed, the introduction of X-ray to PtN$_4$C-SAzyme system resulted in significantly enhanced ROS generation in comparison with the control group (**Figure 4G**), effectively validating their remarkable radiosensitization capacity. Taken together, all these results demonstrated that PtN$_4$C-SAzyme have potential to enhance synergetic CDT and chemo-radiotherapy therapeutic efficiency, resulting from the TME-initiated multiple enzyme-like activities, X-ray-triggered ROS generation, GSH-depletion and Pt^{2+}-releasing capabilities of PtN$_4$C-SAzyme.
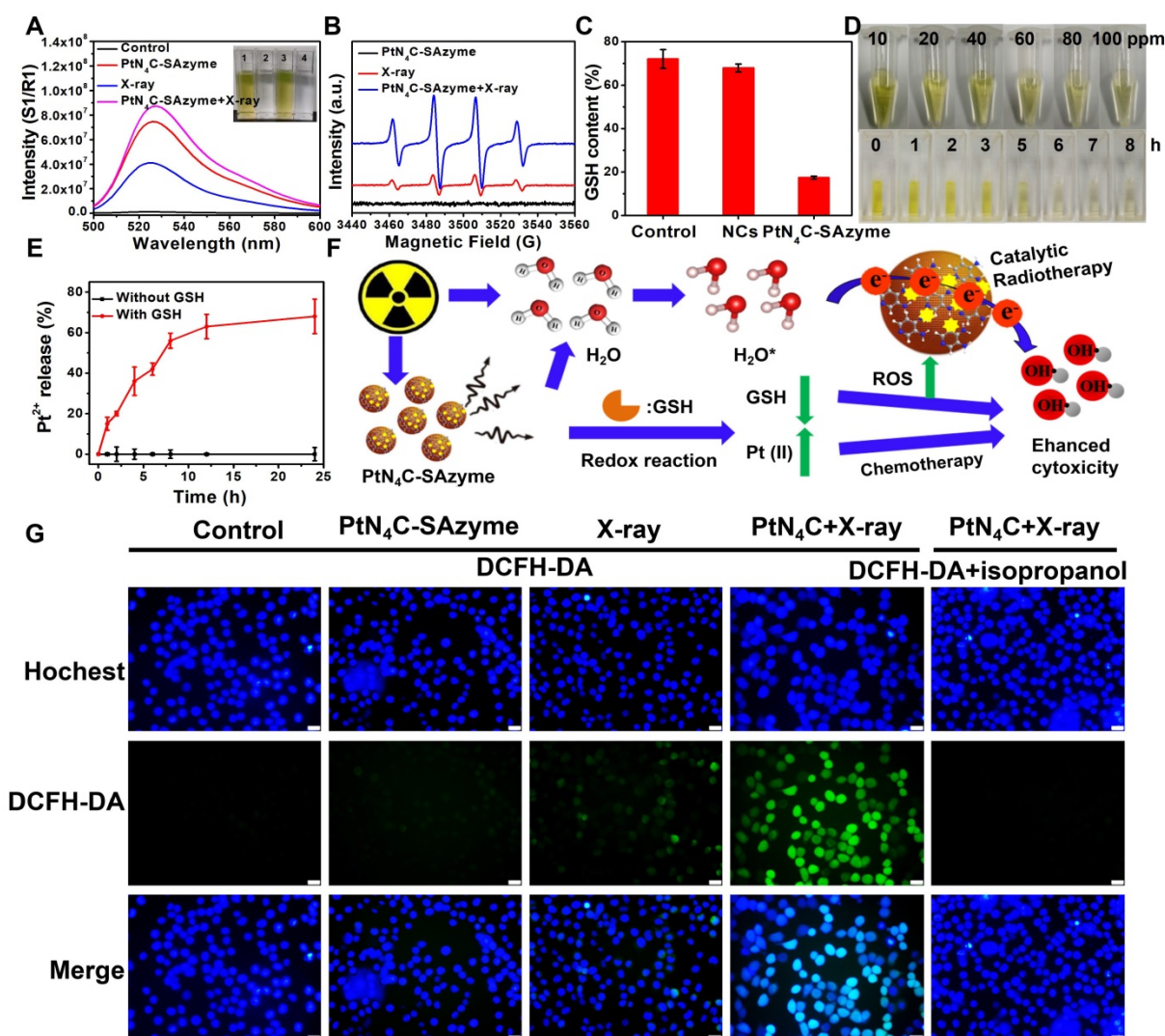

Figure 4. PtN$_4$C-SAzyme-enhanced tumor chemoradiotherapy by generation Pt^{2+} and ROS with the depletion of GSH. (A) Fluorescence spectra of DCFH-DA mixed with PtN$_4$C-SAzyme (100 µg/mL) exposed to X-ray. (B) EPR spectra for the detection of ·OH from PtN$_4$C-SAzyme in the presence or absence of X-ray. (C) Relative content of GSH before and after addition of PtN$_4$C-SAzyme and NCs. (D) Photographs of glutathione oxidation by recording the color change of the solution mixture with the changes in concentration and time. (E) Pt^{2+} release profiles of PtN$_4$C-SAzyme with or without GSH. (F) Mechanism diagram of the reaction. (G) ROS generation of 4T1 cells with different treatments. The scale bar is 100 µm. Error bars were calculated by SD of three parallel samples.

After proving the promising ·OH generation capacity of PtN$_4$C-SAzyme under X-ray irradiation in aqueous solutions, we further substantiated at the cellular level whether the X-ray-triggered ROS generation, GSH-depletion and Pt^{2+}-releasing properties could effectively inhibit cancer cell growth and improve cell killing (**Figure 5A**). As illustrated in **Figure 5B**, their potential chemotherapy performance against 4T1 cells was first evaluated according to the standard cell counting Kit-8 (CCK-8) assay. Compared to untreated cells, the cell viabilities exhibited SAzymes concentration-dependent cytotoxicity. When the PtN$_4$C-SAzyme concentration was 100 μg mL^{-1}, the cell viabilities decreased to 42 %, which might be ascribed to the excellent Fenton-like Pt^{2+} delivery and GSH depletion of PtN$_4$C-SAzyme under intracellular reduction environments. Furthermore, the introduction of X-ray into PtN$_4$C-SAzyme system further promoted cancer cell killing and also exhibited an X-ray dose-dependent toxicity to 4T1 cells for chemoradiotherapy (**Figure 5C**). And the cell live/dead double staining assay indicated that the cell viability of PtN4C-SAzyme+X-ray group is remarkably lower than that of the PtN$_4$C-SAzyme or X-ray alone, (**Figure 5D&S17**), confirming their distinguished synergistic capability of GSH-triggered Pt^{2+} release behavior and local radiation deposition for remarkable ·OH production of synergistic CDT and chemoradiotherapy. It is well known that the intracellular ROS burst may cause multiple damages in chemoradiotherapy, particularly inducing DNA double-strand breaks (DSBs) for causing cell apoptosis or programmed cell death. Therefore, we further explored the underlying mechanisms of PtN$_4$C-SAzyme-mediated enhanced radiosensitization by detecting DNA DSBs with labeling γ-H2AX, a marker of double-stranded DNA breakage with high specificity and accuracy. The results displayed that significantly increased detectable γ-H2AX immunofluorescent spots were observed in the presence of X-rays (6 Gy), particularly in the PtN$_4$C-SAzyme group (**Figure 5E&S18**). However, only few of intranuclear spotty fluorescence from γ-H2AX were discovered without irradiation. And the γ-H2AX immunofluorescent spots of the PtN$_4$C-SAzyme increased by approximately 91.67 % and 84.42 % compared with PBS and PtN$_4$C-SAzyme, respectively, which were calculated via counting the red fluorescent foci (**Figure 5F**), demonstrating PtN$_4$C-SAzyme possessed the admirable therapeutic activity and can cause severe oxidative stress in cancer cells. It was worth noting that short-term CCK-8 assay was uncommon to investigate survival of irradiated cells, clonogenic assay was further conducted to evaluate the enhanced radiotherapy efficiency of the PtN$_4$C-SAzyme for accurate comparison. As shown in **Figure 5G**, the colonies were densely packed in the control group. However, the surviving fractions of the PtN$_4$C-SAzyme groups were relatively lower, indicating that the PtN$_4$C-SAzyme exhibited chemotherapy effect at the experimental concentration and had some effect on cell proliferation. Specifically, the cell survival fraction significantly decreased to 2.7 % after the X-ray irradiation treatment (6 Gy) combined with PtN$_4$C-SAzyme, indicating that the PtN$_4$C-SAzyme was excellent for radiosensitization. Consequently, all these data confirmed that TME-activatable PtN$_4$C-SAzyme with remarkable H$_2$O$_2$ self-supplement, O$_2$-evolving, and GSH depletion-induced Pt^{2+} delivery capacities had great potential application for tumor CDT and chemoradiotherapy.

Encouraged by the intriguing catalytic-therapeutic efficacy of PtN$_4$C-SAzyme *in vitro*, we inferred PtN$_4$C-SAzyme might also have a considerable synergistic CDT and chemoradiotherapy efficacy *in vivo*. In order to prove this point, their enhanced CDT and chemoradiotherapy *in vivo* was investigated in the 4T1 cancer xenograft model using the BALB/c nude mice (**Figure 6A**). The 4T1 tumor-bearing nude mice were randomly divided into five groups, including (i) PBS, (ii) X-ray irradiation, (iii) cisplatin, (iv) PtN$_4$C-SAzyme, (v) PtN$_4$C-SAzyme and X-ray irradiation. As indicated in **Figures 6B-D**, tumor growth in mice treated with PtN$_4$C-SAzyme was significantly suppressed compared with other control groups, especially irradiation with X-ray irradiation, which could be attributed to the X-ray-responsive PtN$_4$C-SAzyme-induced severe oxidative stress. In addition, due to the drug-resistance of cisplatin, the volume of tumor in the cisplatin group was slightly larger than the PtN$_4$C-SAzyme group, manifesting that our PtN$_4$C-SAzyme have remarkable chemotherapy effect for overcoming drug-resistance and suppressing tumor growth. The striking anti-tumor efficacy of PtN$_4$C-SAzyme may be beneficial from the continual accumulation of H$_2$O$_2$, overexpressed GSH depletion-triggered Pt^{2+} release and O$_2$ evolving-induced tumor hypoxia alleviation for *in situ* generating numerous ROS. Following that, the toxicology of PtN$_4$C-SAzyme was systematically investigated to guarantee their safe bioapplication. Encouragingly, no apparent systemic toxicity induced by PtN$_4$C-SAzyme in the presence or absence of X-ray irradiation was observed, as depicted in the major organs, blood biochemistry and hematology analysis (**Figure S19-21**). In addition, all these mice in each group exhibited negligible weight fluctuations (**Figure 6E**), proving the high biocompatibility of PtN$_4$C-SAzyme.

The pathological examination of tumors via hematoxylin and eosin (H&E) staining and Hypoxia-inducible factor 1α (HIF1-α)-mediated immunohistochemical analysis further demonstrated PtN₄C-SAzyme combination with X-ray could sharply augment cancer cell apoptosis by inducing severe oxidative stress and alleviate tumor hypoxia (**Figure 6F**). Therefore, these combined results demonstrated that the utilization of PtN₄C-SAzyme could greatly treated 4T1 tumors with enhanced efficacy and minimized systemic toxicity.
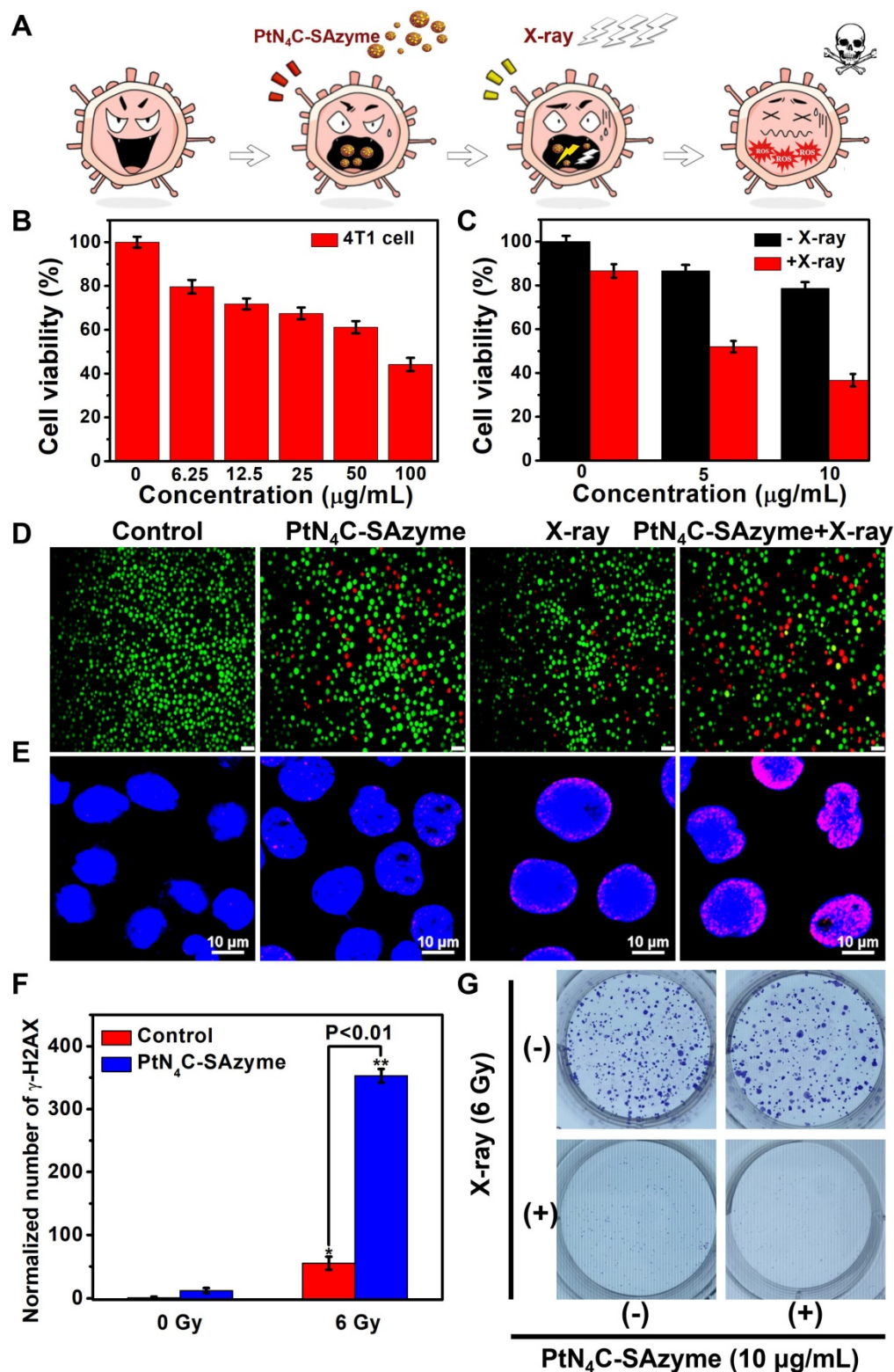

Figure 5. PtN₄C-SAzyme-enhanced CDT and chemoradiotherapy for increased apoptosis and DNA double-strand damage in 4T1 cells. (A) Schematic illustration of 4T1 cell therapeutic outcome by combination PtN₄C-SAzyme with X-ray. (B) Cell viability of 4T1 cell after treated with different concentrations of PtN₄C-SAzyme.

(C) Cell viability of 4T1 cells co-incubated with PtN$_4$C-SAzyme in the presence or absence of X-ray. (D) Live/dead co-staining images of 4T1 cells in different solutions. Scale bar=20 μm. Representative fluorescence images (E) and corresponding normalized number (F) of γ-H2AX of DNA fragmentation and nuclear condensation induced by PtN$_4$C-SAzyme (10 μg/mL, 2 mL) and/or X-ray radiation (6 Gy). (G) Colon formation of 4T1 cells after different treatments. Opposed to (−), (+) denotes X-ray was in the presence of in the group. Error bars were calculated by SD of three parallel samples. P values were based on the Student's test: *P < 0.05, **P < 0.01.
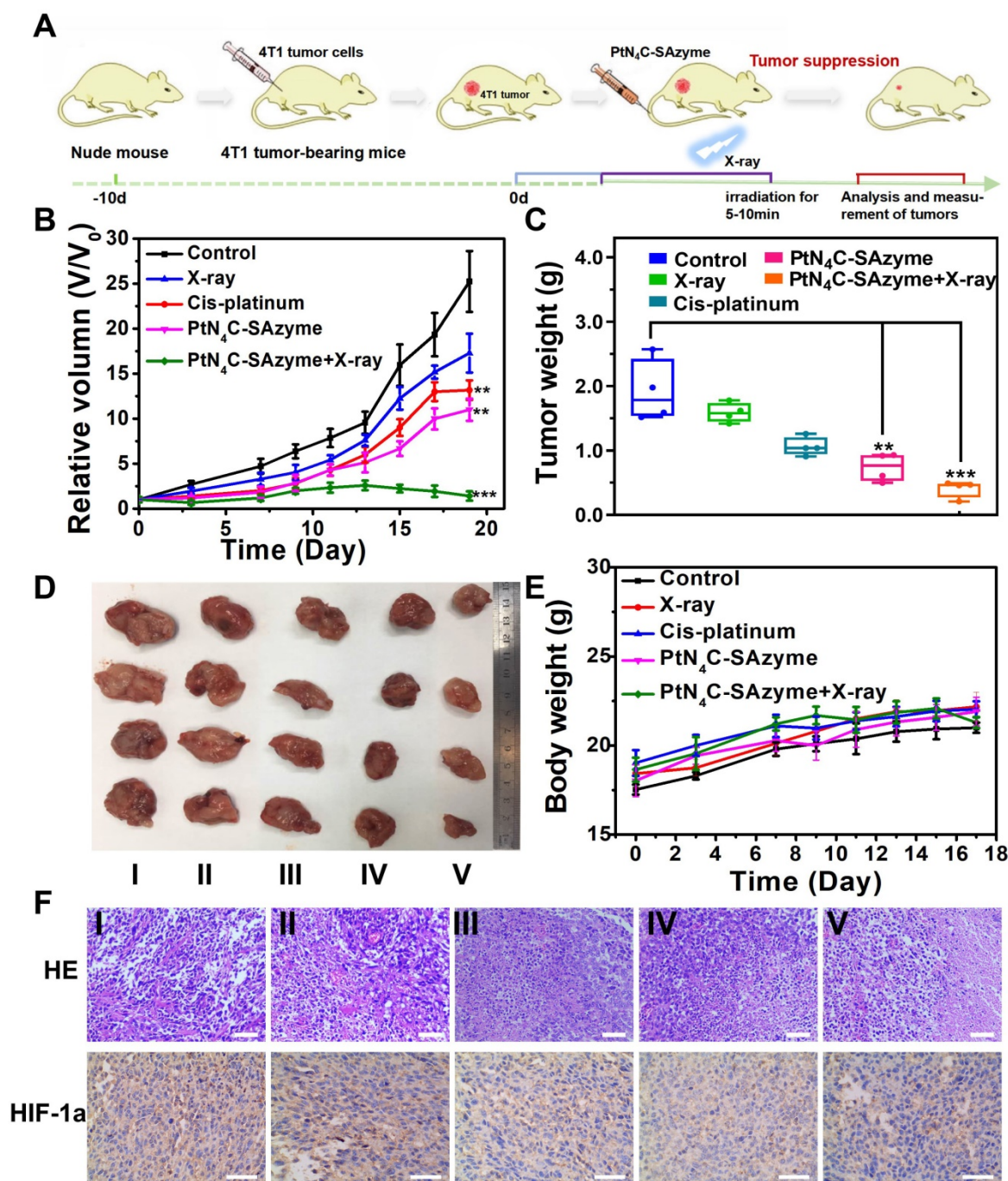

Figure 6. *In vivo X-ray-enhanced PtN$_4$C-SAzyme-based tumor synergistic catalytic therapy against 4T1 tumor xenografts.* (A) Schematic illustration of 4T1 tumor xenograft establishment and therapeutic outcome. Tumor volume (B) and tumor weight changes (C) of 4T1-tumor-bearing mice after different treatments at 19 days. Tumor photographs (D) and weight (E) of mice in different groups after 19 days of treatments. (F) H&E and HIF-1α staining assay of tumor tissues in different groups. Scale bar=50 μm. P values were based on the Student's test: *P < 0.05, **P < 0.01.

Conclusion

In summary, we have successfully developed a specific TME-activated SAzymes-based with parallel cascaded catalytic performance to break through the challenge for intensive CDT and chemoradiothearpy. At the specific microenvironment of tumor, the SAzyme could boost substantial ·OH generation and O$_2$ self-sufficiency for magnifying ROS-involving CDT and O$_2$-dependent chemoradiothearpy effect by their favorable multiple enzyme-like catalytic activities as well as X-ray deposition capacity.

Simultaneously, sustainable GSH consumption and elevated Pt^{2+} release could be achieved *in situ* of tumor by the self-cyclic valence alteration of Pt (IV) and Pt (II) for overwhelming the anti-oxidation defense effect and alleviating drug-resistance of hypoxia tumor. More significantly, the superoxide dismutase-like activity of SAzyme endowed H_2O_2 cyclic accumulation, which could in turn react with PtN_4C-SAzyme to achieve the cyclic blowout of ·OH and O_2, so as to generate a "key" to unlock the multiple enzyme-like activities of SAzymes for tumor-specific cascaded catalytic CDT and chemoradiothearpy. Overall, we anticipate that this TME-inspired strategy will be a strong tool to treatment of various diseases and provide new perspective for us to broaden the biomedical applications of SAzymes.

Experimental Section

Materials

Cisplatin, 3, 4-diaminopyridine (DAP), 3, 3′, 5, 5′-tetramethylbenzidine (TMB), isopropanol, and potassium thiocyanate (KSCN) were purchased from Aladdin Reagent CO, Ltd. (Shanghai, China). Calcein AM and propidium iodide (PI) were obtained from Sigma-Aldrich (USA). Hydrogen peroxide (H_2O_2, 30 %) was ordered form Jinshan chemical reagent Co. Ltd (Chengdu, China). Reduced glutathione (GSH) was obtained from Nanjing jiancheng institute of biological engineering. 4 % paraformaldehyde was bought from Labgic Technology Co, Ltd (Beijing, China). Xanthine (X), Xanthine oxidase (XO), Methylene blue (MB) and Nitro-blue tetrazolium (NBT) were purchased from Sigma-Aldrich, USA. Reactive oxygen species assay kit based on 2, 7-Dichlorodi-hydrofluorescein diacetate (DCFH-DA) was acquired from Beyotime Biotechnology Co, Ltd. Live/Dead dye for viability/cytotoxicity assay was acquired from enzyme-linked Biotechnology Co., Ltd (Shanghai, China). All chemicals were utilized as purchased without further purified.

Characterization

The morphology and composition of samples were characterized by using transmission electron microscope (TEM, FEI, Tecnai, G2 F20, USA) by dropping PtN_4C-SAzyme samples onto a carbon-coated copper grids and drying them naturally before imaging. SEM images were acquired on a Zeiss Sigma 500 FE-SEM (Carl Zeiss AG, Oberkochen, Germany) at a working voltage of 10 kV and working current of 10 μA after 60 s of platinum coating. The X-ray absorption spectra (XAS) including X-ray absorption near-edge structure (XANES) and extended X-ray absorption fine stucture (EXAFS) of

the samples at Pt K-edge (11564 eV) were collected at the Singapore Synchrotron Light Source (SSLS) center, where a pair of chanel-cut Si (111) crystals was used in the monochromator. The Pt K-edge XANES data were recorded in a transmission mode. Pt foil was used as reference. Fourier-transform infrared spectra (FTIR) of PtN_4C-SAzyme was measured on an FT-IR spectrometer (IR 200, Thermo Fisher Scientific, US) with KBr particles in the range region of 4000-500 cm^{-1}. The Raman spectrum of the PtN_4C-SAzyme samples was recorded on a Raman spectrophotometer (Invia Reflex, Renishaw, UK). The optical characterizations of PtN_4C-SAzyme were performed using a UV-vis spectrometer (UV-6100, Mapada, China) with a 1 cm cuvette. X-ray photoelectron spectroscopy (XPS) analysis was monitored using an ESCALAB 250 X-ray photoelectron spectrometer. X-ray diffractometry using Cu-Kα radiation (λ=0.15405 nm) was used to obtain crystallographic information. Zetasizer (Malvern, UK) was used to acquire the size distribution and ζ-potential of the as-synthesized PtN_4C-SAzyme. Fluorescence spectra were obtained on a dual-FL luminescence spectrometer (HORIBA, Japan). The cells images were recorded using an inverted fluorescence microscope (Axio Vert.A1, Zeiss, Germany). The concentration of Pt^{2+} was quantitated using the inductively coupled plasma mass spectrometry (ICP-MS, Thermo Elemental X7).

Synthesis of prodrug

The described method was according to a reported strategy by Jiang et al [68, 69]. In detail, dried cis-$[PtCl_2(NH_3)_2]$ (0.4 g, 0.6 mmol) was suspended in water (14 mL) and a 10-fold excess of 30 % H_2O_2 (14 mL, 6 mmol) was then added, and the mixed system was reacted at 50 °C for 1 h. The obtained yellow solution was recrystallized, extracted and filtered to obtain crystals. Then, the crystals were washed sequentially with cold water, ethanol and ether, and finally dried in a desiccator to obtain a yellow solid powder (cis-$[PtCl_2(OH)_2(NH_3)_2]$). Whereafter, 0.2 g of the yellow solid powder obtained above (cis-$[PtCl_2(OH)_2(NH_3)_2]$) was dissolved in HCl (5 mL, 10 mol/L) at 50 °C and stirring for 1 h. After that, the above reaction system was moved away for continually stirring for 8 h at room temperature again to obtain a light yellow cisplatin precursor drug solution (cis-$PtCl_4(NH_3)_2$), which was sealed and stored at room temperature.

Synthesis of PtN₄C-SAzyme

The method was according to a reported strategy with a slight modification [68, 69]. Briefly, 25 mL of water and 0.13 g of 3, 4-diaminopyridine (DAP) were

added into the previously obtained yellowish solution (cis-PtCl$_4$(NH$_3$)$_2$) and the reaction was stirred for 24 h at 37 °C. After cooling down to room temperature, the resulting light red solution was acquired after purification through dialysis bag with cut-off 12 kDa MW for 5 h to remove the impurities and finally freeze-dried to obtain a dried sample powder for further use.

Atomic structure analysis of PtN$_4$C-SAzyme

The obtained extended X-ray absorption fine structure (EXAFS) data were manipulated according to a standard procedure using the ATHENA model implemented in the IFEFFIT software packages [71]. Subsequently, the k3-weighted EXAFS spectra was acquired by the background at the post-edge from the overall absorption and then normalized with regard to the edge-jump step. The k3-weighted χ(k) data at the Pt L3-edge were then Fourier transformed into real (R) space by using a hanning windows (dk = 1.0 Å^{-1}) to separate the EXAFS contributions from the various coordination shells. To acquire the quantitative structural parameters around the central atom, least-squares curve parameter fitting was conducted by using the ARTEMIS module of IFEFFIT software packages.

Density functional theory (DFT) calculation

All the calculations were conducted within the framework of the density functional theory (DFT) as implemented in the Vienna Ab initio Software Package (VASP 5.3.5) code using the Perdew-Burke-Ernzerhof (PBE) generalized gradient approximation of the projected augmented wave (PAW) approach [77]. The cutoff energy of the plane-wave fundamental was set at 400 eV. The Brillouin zone of the surface unit cell was simulated by a Monkhorst-Pack (MP) grid, and the k-point grid was used for structural optimization of Pt-N-doped graphene catalysts. The catalyst surface was decided by a 3×3×1 Monkhorst-Pack grid. The electronic self-consistent iteration and force convergence criteria were set to 10^{-5} eV and 0.01 eV/Å, respectively. In this work, we constructed a 3×2 catalyst surface supercell including 1 atomic layer to simulate Pt-N-doped graphene catalysts. A vacuum layer of 12 Å was introduced to prevent interactions between periodic images. The absorption energy (E$_{ads}$) of the surface species is defined by E$_{ads}$=E$_{total}$-E$_{surface}$-E$_{species}$, where E$_{total}$ denotes the total energy absorbed by the catalyst surface, E$_{surface}$ denotes the energy of the empty surface, and E$_{species}$ denotes the energy of the surface species in the gas phases.

Peroxidase-like activity of PtN$_4$C-SAzyme

The peroxidase-like activity of PtN$_4$C-SAzyme

was determined by UV-vis spectrometer (UV-6100, Mapada, China) after 30 min reaction. The absorbance of oxTMB at the characteristic peak of 652 nm was recorded by a UV-vis spectrometer for a certain reaction time to investigate the peroxidase-like activity of PtN$_4$C-SAzyme. Four groups were divided: (i) Control, (ii) H$_2$O$_2$, (iii) PtN$_4$C-SAzyme, (iv) PtN$_4$C-SAzyme+H$_2$O$_2$. Typically, a quantified PtN$_4$C-SAzyme, TMB (0.5 mM), and H$_2$O$_2$ (50 mM) were added to the NaAc buffer (pH = 4), successfully. To explore the optimal conditions of TMB oxidation by PtN$_4$C-SAzyme, a range of temperatures (25, 30, 35, 40, 50, 60, 70 °C) and pH values as well as various H$_2$O$_2$ concentrations were used for the reactions under all other same conditions.

The apparent kinetic parameters were calculated by the Lineweaver-Burk double reciprocal equation derived from the Michaelis-Menten equation:

$$\frac{1}{v} = \frac{K_m}{V_{max}[s]} + \frac{1}{V_{max}}$$

where v is the initial velocity, V$_{max}$ is the maximal reaction velocity, [s] is the concentration of substrate and K$_m$ is the Michaelis constant. The steady-state kinetic assays were performed at NaAc reaction buffer solution with PtN$_4$C-SAzyme solution (100 µg/mL), H$_2$O$_2$, and TMB. To explore this mechanism, the Michaelis-Menten constants were obtained from adjusting different concentrations of TMB and H$_2$O$_2$ under the standard reaction conditions described above. In addition, MB was also used as a probe to investigate the ·OH generation by the Fenton-like reaction of PtN$_4$C-SAzyme. In the first place, MB (10 µg/mL), PtN$_4$C-SAzyme (100 µg/mL) and H$_2$O$_2$ (10 mM) were added sequentially in NaHCO$_3$/5 % CO$_2$ buffer solution (25 mM), and then the mixture stood still at 37 °C for 30 min protected from light. Then, the ·OH-induced decomposition of MB was detected by variation in absorption at 665 nm.

Catalase-like activity of PtN$_4$C-SAzyme

The catalase-like activities of PtN$_4$C-SAzyme were measured by recording the generated oxygen at room temperature using a portable dissolved oxygen meter. In a typical test, 100 µg/mL of PtN$_4$C-SAzyme (5 mL) and 100 µL 30 % H$_2$O$_2$ (0.5, 1, 2 mM) solution was added into the 44.9 mL of buffer solution (0.1 M NaOAc buffer, pH = 7.0), successively. The content of dissolved oxygen was monitored by using a dissolved-oxygen meter over 10 min (mg/L).

Superoxide dismutase-like activity of PtN$_4$C-SAzyme

The superoxide dismutase-like activities of PtN$_4$C-SAzyme were evaluated by the classic

nitroblue tetrazolium (NBT) chromogenic method. An O_2^--sensitive NBT probe was used to assess the superoxide dismutase-like activity of PtN$_4$C-SAzyme. First, different concentrations of PtN$_4$C-SAzyme were incubated with X (1 mM) and XO (0.05 U/mL) in Tris-HCl buffer (0.1 M, pH = 7.5) at 37 °C for 5 min. Then, NBT (100 μg/mL) was incorporated into the mixed solution and their absorbance at the characteristic peak of 550 nm was continuously monitored over 5 min using a UV-vis spectrometer. The complete reaction assembly was closed in a foil-lined box. Saline was used as a negative control and O_2^--sensitive NBT solution without PtN$_4$C-SAzyme was used as a positive control. The inhibition rate was computed by the following formula: inhibition (%) = $[(A_0-A)/A_0] \times 100$ %, where A_0 is the absorption of the control and A is the absorption of the sample.

GSH and H$_2$O$_2$ consumption

Extracellular GSH consumption was measured by a Glutathione Reductase Assay Kit with DTNB (Nanjing Jiancheng Bioengineering Institute, China). Firstly, PBS solution (pH = 7.4) containing PtN$_4$C-SAzyme (100 μg/mL) and GSH (50 μM) were coincubated in a shaker at 25 °C for different times (1, 2, 3, 4, 5, 6, 7, 8 h). Afterward, these mixtures were centrifuged at 12000 rpm for 15 min to obtain the corresponding supernatants. The absorbance of corresponding supernatants solution was measured by a UV-vis spectrometer at 412 nm. In addition, the H$_2$O$_2$ concentration was evaluated using the H$_2$O$_2$ Assay Kit (Nanjing Jiancheng Bioengineering Institute, China). In brief, two groups were divided, which included H$_2$O$_2$ and PtN$_4$C-SAzyme + H$_2$O$_2$. 0.1 mL of SAzyme sample or standard was combined with 1 mL of reagent I and reagent II, respectively and the absorption of mixed solution was measured at 405 nm.

Detection of reactive oxygen species produced by PtN$_4$C-SAzyme under X-ray irradiation

Firstly, 0.5 mL of DCFH-DA in DMSO was combined with 2 mL of NaOH (0.01 M) at room temperature and the mixtures were chemically hydrolyzed to DCFH. After 30 min, 10 mL of phosphate buffer (PBS, 25 mM, pH 7.2) was inserted and the resulted DCFH solution was covered with aluminum foil and placed on ice for further experiments. Subsequently, PtN$_4$C-SAzyme (100 μg/mL) was mixed with DCFH (10 μM) solution in the absence or presence of GSH (1 mM) and then irradiated with X-rays for 10 min. Finally, the fluorescence of the solution was measured to assess the generated ROS.

Intracellular free radical production

The intracellular ROS production was investigated by the chemical probe 2, 7-Dichlorodi-hydrofluorescein diacetate (DCFH-DA), which could be oxygenated by the generated ROS and emits green fluorescence. The 4T1 cells were inserted into 12-well plates and grown with adhesion on the walls. The cells were further incubated for 6 h in the addition of fresh medium containing PtN$_4$C-SAzyme (100 μg/mL). After washing three times with PBS, 4T1 cells were exposed to X-ray (6 Gy) for 5 min. Then, DCFH-DA was added and incubated with 4T1 cells for another 30 min. the production of ROS could be observed by CLSM.

Measurement of cytotoxicity in PtN$_4$C-SAzyme

The cytotoxicity of PtN$_4$C-SAzyme was evaluated by the standard Cell Counting Kit-8 (CCK-8). The 4T1 cells were placed in 96-well plates at a density of 4×10^3 cells per well and incubated in a humidified incubator (37 °C, 5% CO$_2$) for 24 h. Each well was then washed with PBS (10 mM, pH = 7.4) and different concentrations of PtN$_4$C-SAzyme (0, 6.25, 12.5, 25, 50, and 100 μg/mL) were added. The cells were then coincubated for 24 h. 10 μL of CCK-8 was subsequently added to each well and kept in the incubator for another 1 h. Finally, cell viability was assessed by absorbance at 450 nm using a microplate reader (Thermo Scientific, Multiscan MNK3). Cells without PtN$_4$C-SAzyme were treated as controls, and cell viability was calculated relative to control cells.

In vitro clonogenic survival assays and detection of DNA double-strand breaks

To measure the sensitivity to DNA damaging agents, clonogenic survival assays were performed. The 4T1 cells were seeded at 1000 cells/well into 24-well plates and cultured for 24 hours. Then, the cells were divided into 4 groups including (I) Control (without treatment), (II) PtN$_4$C-SAzyme, (III) X-ray, (IV) PtN$_4$C-SAzyme+X-ray (6 Gy). The cells after different treatments were further cultured for 10 days and then the colonies were stained with Giemsa dye and the survival rate of the colonies was used to assess the effect of the different treatments. To further test for DNA double-strand breaks, 4T1 cells were cultured at a density of 3×10^4 cells per well in a 35 mm confocal plate. After 24 h, the cells were divided into four treatment groups: (I) Control (without treatment), (II) PtN$_4$C-SAzyme, (III) X-ray, (IV) PtN$_4$C-SAzyme+X-ray (6 Gy). The Cells were fixed with 4 % paraformaldehyde (10 min) after 24 h of culture and permeabilized with 0.2 % Triton X-100 (10 min). Next, to prevent their interaction with

nonspecific proteins, 4T1 cells were treated with 5% FBS for 1 h. The cells were previously incubated with anti-phospho-histone H2A.X (ser139) overnight at 4 °C, followed by Anti-rabbit IgG (H+L) for 1 h. Hoechst was used to stain the nuclei of the cells. DNA was shown in red and phospho-histone H3 (PH3) in green. Finally, the cells were imaged under a confocal laser scanning microscope after washing.

In vivo antitumor efficiency evaluation

All the experimental protocols were approved by Sichuan Provincial Centers for Disease Prevention & Control. Mice bearing 4T1 breast tumors were randomly classified into five groups: (I) Control (without treatment); (II) X-ray; (III) cisplatin; (IV) PtN$_4$C-SAzyme; (V) PtN$_4$C-SAzyme+X-ray. Each group contained four mice respectively. When the tumor volume of mice reached 75 mm^3, 20 μL of saline or PtN$_4$C-SAzyme (2 mg/mL, 20 μL) were injected subcutaneously in the right leg of nude mice with 4T1 mammary carcinoma into the body for 24 h. It was notable that the concentration of platinum ions in the third and fourth groups was consistent. The mice were exposed to X-rays (6 Gy) for 5 min. The changes in body weight and tumor volume were recorded for 20 days during treatment. The tumor growth is measured by calculated as follows: V= W^2×L/2, where L and W stand for the length and width of the tumor, respectively. The relative tumor volume was V/V$_0$, where V indicates the tumor volume on various days and V$_0$ represents the first day's tumor volume. Meanwhile, the body weight of mice was measured every other day. Finally, mice were sacrificed and tumors and major organ tissues from five groups were collected for hematoxylin and eosin (H&E) staining, and blood was collected from the fundus arteriosus of each group of mice for routine blood and blood biochemical tests. Animal studies were conducted in compliance with the guidelines of the Institutional Animal Care and Use Committee. The mice were discarded according to the standard approved protocol after we finished the experiment.

Histological analysis

After treatment, mice were sacrificed and tumors and major organ tissues (heart, liver, spleen, lung, kidney) were collected from each group of mice, fixed in 4 % paraformaldehyde, and embedded in paraffin. 5 μm sections were taken, and the sections were examined histopathologically with hematoxylin and eosin (H&E). In addition, blood was collected from the fundus artery of each group of mice for routine blood and blood biochemical examination.

Statistical analysis

All the experiments completed accomplished in triplicate. The data obtained were expressed as the mean value ± standard deviation, and the Student's t-test was performed to analyze the statistical significance between two groups. *p < 0.05 was considered statistically significant and **p < 0.01 means extremely significant.

Supplementary Material

Supplementary figures.
https://www.thno.org/v12p5155s1.pdf

Competing Interests

The authors have declared that no competing interest exists.

References

1. Poyton M F, Sendecki A M, Cong X, Cremer P S. Cu^{2+} binds to phosphatidylethanolamine and increases oxidation in lipid membranes. J Am Chem Soc. 2016; 138: 1584-90.
2. Tang Z, Zhang H, Liu Y, Ni D, Zhang H, Zhang J, et al. Antiferromagnetic pyrite as the tumor microenvironment-mediated nanoplatform for self-enhanced tumor imaging and therapy. Adv Mater. 2017; 29: 1701683.
3. Zhang C, Bu W, Ni D, Zhang S, Li Q, Yao Z, et al. Synthesis of iron nanometallic glasses and their application in cancer therapy by a localized fenton reaction. Angew Chem Int Ed Engl. 2016; 55: 2101-6.
4. Tian Q, Xue F, Wang Y, Cheng Y, An L, Yang S, et al. Recent advances in enhanced chemodynamic therapy strategies. Nano Today. 2021; 39:101162.
5. Tang Z, Liu Y, He M, Bu W. Chemodynamic therapy: tumour microenvironment-mediated fenton and fenton-like reactions. Angew Chem Int Ed Engl. 2019; 58: 946-56.
6. Lin H, Chen Y, Shi J. Nanoparticle-triggered *in situ* catalytic chemical reactions for tumour-specific therapy. Chem Soc Rev. 2018; 47: 1938-58.
7. Ma B, Wang S, Liu F, Zhang S, Duan J, Li Z, et al. Self-assembled copper-amino acid nanoparticles for *in situ* glutathione "AND" H$_2$O$_2$ sequentially triggered chemodynamic therapy. J Am Chem Soc. 2019; 141: 849-57.
8. Yang B, Chen Y, Shi J. Nanocatalytic Medicine. Adv Mater. 2019; 31: e1901778.
9. Zhang C, Yan L, Wang X, Dong X, Zhou R, Gu Z, et al. Tumor microenvironment-responsive Cu$_2$(OH)PO$_4$ nanocrystals for selective and controllable radiosentization via the X-ray-triggered fenton-like reaction. Nano Lett. 2019; 19: 1749-57.
10. Xu C, Yuan Z, Kohler N, Kim J, Chung M A, Sun S. FePt nanoparticles as an Fe reservoir for controlled Fe release and tumor inhibition. J Am Chem Soc. 2009; 131: 15346-51.
11. Dixon S J, Stockwell B R. The role of iron and reactive oxygen species in cell death. Nat Chem Biol. 2014; 10: 9-17.
12. Kim S E, Zhang L, Ma K, Riegman M, Chen F, Ingold I, et al. Ultrasmall nanoparticles induce ferroptosis in nutrient-deprived cancer cells and suppress tumour growth. Nat Nanotechnol. 2016; 11: 977-85.
13. Ma P, Xiao H, Yu C, Liu J, Cheng Z, Song H, et al. Enhanced cisplatin chemotherapy by iron oxide nanocarrier-mediated generation of highly toxic reactive oxygen species,. Nano Lett. 2017; 17: 928-37.
14. Zheng D, Lei Q, Zhu J, Fan J, Li C, Li C, et al. Switching apoptosis to ferroptosis: metal-organic network for high-efficiency anticancer therapy, Nano Lett. 17 (2017) 284-291.
15. Huo M, Wang L, Chen Y, Shi J. Tumor-selective catalytic nanomedicine by nanocatalyst delivery. Nat Commun. 2017; 8: 357.
16. Sang Y, Cao F, Li W, Zhang L, You Y, Deng Q, et al. Bioinspired construction of a nanozyme-based H$_2$O$_2$ homeostasis disruptor for intensive chemodynamic therapy. J Am Chem Soc. 2020; 142: 5177-83.
17. Xu B, Cui Y, Wang W, Li S, Lyu C, Wang S, et al. Immunomodulation-enhanced nanozyme-based tumor catalytic therapy. Adv Mater. 2020; 32: e2003563.

18. Lin L, Song J, Song L, Ke K, Liu Y, Zhou Z, et al. Simultaneous fenton-like ion delivery and glutathione depletion by MnO₂-based nanoagent to enhance chemodynamic therapy. Angew Chem Int Ed Engl. 2018; 57: 4902-6.

19. Kuppusamy P, Li H, Ilangovan G, Cardounel A J, Zweier J L, Yamada K, et al. Noninvasive imaging of tumor redox status and its modification by tissue glutathione levels. Cancer Res. 2002; 62: 307-12.

20. Diehn M, Cho R W, Lobo N A, Kalisky T, Dorie M J, Kulp A N, et al. Association of reactive oxygen species levels and radioresistance in cancer stem cells. Nature. 2009; 458: 780-3.

21. Kumar R, Shin W S, Sunwoo K, Kim W Y, Koo S, Bhuniya S, et al. Small conjugate-based theranostic agents: an encouraging approach for cancer therapy. Chem Soc Rev. 2015; 44: 6670-83.

22. Dong S, Dong Y, Jia T, Liu S, Liu J, Yang D, et al. GSH-depleted nanozymes with hyperthermia-enhanced dual enzyme-mimic activities for tumor nanocatalytic therapy. Adv Mater. 2020; 32: 2002439.

23. Zhao R, Zhang R, Feng L, Dong Y, Zhou J, Qu S, et al. Constructing virus-like SiOx/CeO₂/VOx nanozymes for 1064 nm light-triggered mild-temperature photothermal therapy and nanozyme catalytic therapy. Nanoscale. 2022; 14: 361-72.

24. Ge M, Xu D, Chen Z, Wei C, Zhang Y, Yang C, et al. Magnetostrictive-piezoelectric-triggered nanocatalytic tumor therapy. Nano Lett. 2021; 21: 6764-72.

25. Chang M, Hou Z, Wang M, Yang C, Wang R, Li F, et al. Single-atom Pd nanozyme for ferroptosis-boosted mild-temperature photothermal therapy. Angew Chem Int Ed Engl. 2021; 133: 13081-9.

26. Sun Q, Wang Z, Liu B, He F, Gai S, Yang P, et al. Recent advances on endogenous/exogenous stimuli-triggered nanoplatforms for enhanced chemodynamic therapy. Coord Chem Rev. 2022; 451: 214267.

27. Wang M, Chang M, Chen Q, Wang D, Li C, Hou Z, et al. Au₂Pt-PEG-Ce6 nanoformulation with dual nanozyme activities for synergistic chemodynamic therapy/phototherapy. Biomaterials. 2020; 252: 120093.

28. Qin L, Gan J, Niu D, Cao Y, Duan X, Qin X, et al. Interfacial-confined coordination to single-atom nanotherapeutics. Nat Commun. 2022; 13: 91.

29. Liang X, Chen M, Bhattarai P, Hameed S, Dai Z. Perfluorocarbon@Porphyrin nanoparticles for tumor hypoxia relief to enhance photodynamic therapy against liver metastasis of colon cancer. ACS Nano. 2020; 14: 13569-83.

30. Liu C, Wang D, Zhang S, Cheng Y, Yang F, Xing Y, et al. Biodegradable biomimetic copper/manganese silicate nanospheres for chemodynamic/photodynamic synergistic therapy with simultaneous glutathione depletion and hypoxia relief. ACS Nano. 2019; 13: 4267-77.

31. Xia D, Hang D, Li Y, Jiang W, Zhu J, Ding Y, et al. Au-hemoglobin loaded platelet alleviating tumor hypoxia and enhancing the radiotherapy effect with low-dose X-ray. ACS Nano. 2020; 14: 15654-68.

32. Zhou T, Liang X, Wang P, Hu Y, Qi Y, Jin Y, et al. A hepatocellular carcinoma targeting nanostrategy with hypoxia-ameliorating and photothermal abilities that, combined with immunotherapy, inhibits metastasis and recurrence. ACS Nano. 2020; 14: 12679-96.

33. Fan J, Peng M, Wang H, Zheng H, Liu Z, Li C, et al. Engineered bacterial bioreactor for tumor therapy via Fenton-like reaction with localized H₂O₂ generation. Adv Mater. 2019; 31: e1808278.

34. Feng W, Han X, Wang R, Gao X, Hu P, Yue W, et al. Nanocatalysts-augmented and photothermal-enhanced tumor-specific sequential nanocatalytic therapy in both NIR-I and NIR-II biowindows. Adv Mater. 2019; 31: e1805919.

35. Li W, Su C, Chang Y, Lin Y, Yeh C. Ultrasound-induced reactive oxygen species mediated therapy and imaging using a Fenton reaction activable polymersome. ACS Nano. 2016; 10: 2017-27.

36. Lin L, Huang T, Song J, Ou X, Wang Z, Deng H, et al. Synthesis of copper peroxide nanodots for H₂O₂ self-supplying chemodynamic therapy. J Am Chem Soc. 2019; 141: 9937-45.

37. Zhang L, Wan S, Li C, Xu L, Cheng H, Zhang X. An adenosine triphosphate-responsive autocatalytic Fenton nanoparticle for tumor ablation with self-supplied H₂O₂ and acceleration of Fe(III)/Fe(II) conversion. Nano Lett. 2018; 18: 7609-18.

38. Rankin E-B, Giaccia A-J. Hypoxic control of metastasis. Science. 2016; 352: 175-80.

39. Erler J T, Bennewith K L, Nicolau M, Dornhofer N, Kong C, Le Q-T, et al. Lysyl oxidase is essential for hypoxia-induced metastasis. Nature. 2006; 440: 1222-6.

40. Gilkes D M, Semenza G L, Wirtz D. Hypoxia and the extracellular matrix: drivers of tumour metastasis. Nat Rev Cancer. 2014; 14: 430-9.

41. Song X, Feng L, Liang C, Yang K, Liu Z. Ultrasound triggered tumor oxygenation with oxygen-shuttle nanoperfluorocarbon to overcome hypoxia-associated resistance in cancer therapies. Nano Lett. 2016; 16: 6145-53.

42. Fan W, Yung B, Huang P, Chen X. Nanotechnology for multimodal synergistic cancer therapy. Chem Rev. 2017; 117: 13566-638.

43. Milas L, Mason K A, Liao Z, Ang K K. Chemoradiotherapy: emerging treatment improvement strategies. Head Neck. 2003; 25: 152-67.

44. Son K J, Yoon H-J, Kim J-H, Jang W-D, Lee Y, Koh W-G. Photosensitizing hollow nanocapsules for combination cancer therapy. Angew Chem Int Ed Engl. 2011; 50: 11968-71.

45. He Z, Huang X, Wang C, Li X, Liu Y, Zhou Z, et al. A Catalase-like metal-organic framework nanohybrid for O₂-Evolving synergistic chemoradiotherapy. Angew Chem Int Ed Engl. 2019; 58: 8752-6.

46. Ni K, Lan G, Song Y, Hao Z, Lin W. Biomimetic nanoscale metal-organic framework harnesses hypoxia for effective cancer radiotherapy and immunotherapy. Chem Sci. 2020; 11: 7641-53.

47. Chen Q, Feng L, Liu J, Zhu W, Dong Z, Wu Y, et al. Intelligent albumin-MnO₂ nanoparticles as pH-/H₂O₂-responsive dissociable nanocarriers to modulate tumor hypoxia for effective combination therapy. Adv Mater. 2016; 28: 7129-36.

48. Jia Q, Ge J, Liu W, Zheng X, Chen S, Wen Y, et al. A magnetofluorescent carbon dot assembly as an acidic H₂O₂-driven oxygenator to regulate tumor hypoxia for simultaneous bimodal imaging and enhanced photodynamic therapy. Adv Mater. 2018; 30: e1706090.

49. Liu H, Cheng R, Dong X, Zhu S, Zhou R, Yan L, et al. BiO₂-x nanosheets as radiosensitizers with catalase-like activity for hypoxia alleviation and enhancement of the radiotherapy of tumors. Inorg Chem. 2020; 59: 3482-93.

50. Guo Z, Zhu S, Yong Y, Zhang X, Dong X, Du J, et al. Synthesis of BSA-Coated BiOI@Bi₂S₃ semiconductor heterojunction nanoparticles and their applications for radio/photodynamic/photothermal synergistic therapy of tumor. Adv Mater. 2017; 29: 1704136.

51. Yong Y, Cheng X, Bao T, Zu M, Yan L, Yin W, et al. Tungsten sulfide quantum dots as multifunctional nanotheranostics for *in vivo* dual-modal image-guided photothermal/radiotherapy synergistic therapy. ACS Nano. 2015; 9: 12451-63.

52. Du J, Gu Z, Yan L, Yong Y, Yi X, Zhang X, et al. Poly(vinylpyrrolidone)-and selenocysteine-modified Bi₂Se₃ nanoparticles enhance radiotherapy efficacy in tumors and promote radioprotection in normal tissues. Adv Mater. 2017; 29: 1701268.

53. Yong Y, Zhang C, Gu Z, Du J, Guo Z, Dong X, et al. Polyoxometalate-based radiosensitization platform for treating hypoxic tumors by attenuating radioresistance and enhancing radiation response. ACS Nano. 2017; 11: 7164-76.

54. Li S, Shang L, Xu B, Wang S, Gu K, Wu Q, et al. A Nanozyme with photo-enhanced dual enzyme-like activities for deep pancreatic cancer therapy. Angew Chem Int Ed Engl. 2019; 58: 12624-31.

55. Singh N, Mugesh G. CeVO₄ nanozymes catalyze the reduction of dioxygen to water without releasing partially reduced oxygen species. Angew Chem Int Ed Engl. 2019; 58: 7797-801.

56. Xu Y, Fei J, Li G, Yuan T, Xu X, Li J. Nanozyme-catalyzed cascade reactions for mitochondria-mimicking oxidative phosphorylation. Angew Chem Int Ed Engl. 2019; 58: 5572-6.

57. Gao L, Zhuang J, Nie L, Zhang J, Zhang Y, Gu N, et al. Intrinsic peroxidase-like activity of ferromagnetic nanoparticles. Nat Nanotechnol. 2007; 2: 577-83.

58. Huang Y, Ren J, Qu X. Nanozymes: classification, catalytic mechanisms, activity regulation, and applications. Chem Rev. 2019; 119: 4357-412.

59. Wang X, Gao X J, Qin L, Wang C, Song L, Zhou Y-N, et al. eg occupancy as an effective descriptor for the catalytic activity of perovskite oxide-based peroxidase mimics. Nat Commun. 2019; 10: 704.

60. Wei H, Wang E. Nanomaterials with enzyme-like characteristics (nanozymes): next-generation artificial enzymes. Chem Soc Rev. 2013; 42: 6060-93.

61. Wu J, Wang X, Wang Q, Lou Z, Li S, Zhu Y, et al. Nanomaterials with enzyme-like characteristics (nanozymes): next-generation artificial enzymes (II). Chem Soc Rev. 2019; 48: 1004-76.

62. Jiao L, Yan H, Wu Y, Gu W, Zhu C, Du D, et al. When nanozymes meet single-atom catalysis. Angew Chem Int Ed Engl. 2020; 59: 2565-76.

63. Huo M, Wang L, Wang Y, Chen Y, Shi J. Nanocatalytic tumor therapy by single-atom catalysts. ACS Nano. 2019; 13: 2643-53.

64. Zhu Y, Wang W Y, Cheng J J, Qu Y T, Dai Y, Liu M M, et al. Stimuli-responsive manganese single-atom nanozyme for tumor therapy via integrated cascade reactions. Angew Chem Int Ed Engl. 2021; 60: 9480-8.

65. Wang D, Wu H, Phua S Z F, Yang G, Qi Lim W, Gu L, et al. Self-assembled single-atom nanozyme for enhanced photodynamic therapy treatment of tumor. Nat Commun. 2020; 11: 357.

66. Wang D, Wu H, Wang C, Gu L, Chen H, Jana D, et al. Self-assembled single-site nanozyme for tumor-specific amplified cascade enzymatic therapy. Angew Chem Int Ed Engl. 2021; 60: 3001-7.

67. Xiang H, Feng W, Chen Y. Single-atom catalysts in catalytic biomedicine. Adv Mater. 2020; 32: e1905994.

68. Bai J, Jia X, Zhen W, Cheng W, Jiang X. A facile ion-doping strategy to regulate tumor microenvironments for enhanced multimodal tumor theranostics. J Am Chem Soc. 2017; 140: 106-9.

69. Hall M D, Dillon C T, Zhang M, Beale P, Cai Z, Lai B, et al. The cellular distribution and oxidation state of platinum (II) and platinum (IV) antitumour complexes in cancer cells. J Biol Inorg Chem. 2003; 8: 726-32.

70. Jia L, Pang M, Fan M, Tan X, Wang Y, Huang M, et al. A pH-responsive pickering nanoemulsion for specified spatial delivery of immune checkpoint inhibitor and chemotherapy agent to tumors. Theranostics. 2020; 10: 9956-69.

71. Zeng R, Wang W, Cai G, Huang Z, Tao J, Tang D, et al. Single-atom platinum nanocatalyst-improved catalytic efficiency with enzyme-DNA supermolecular architectures. Nano Energy. 2020; 74: 104931.

72. Yan H, Lin Y, Wu H, Zhang W, Sun Z, Cheng H, et al. Bottom-up precise synthesis of stable platinum dimers on graphene. Nat Commun. 2017; 8: 1070.

73. Yin X, Wang H, Tang S, Lu X, Shu M, Si R, et al. Engineering the coordination environment of single-atom platinum anchored on graphdiyne for optimizing electrocatalytic hydrogen evolution. Angew Chem Int Ed Engl. 2018; 57: 9382-6.

74. Liu L, Diaz U, Arenal R, Agostini G, Concepcion P, Corma A. Generation of subnanometric platinum with high stability during transformation of a 2D zeolite into 3D. Nat Mater. 2017; 16: 132-8.

75. Liu J, Jiao M, Lu L, Barkholtz H M, Li Y, Wang Y, et al. High performance platinum single atom electrocatalyst for oxygen reduction reaction. Nat Commun. 2017; 8: 15938.

76. Zhang Z, Zhu Y, Asakura H, Zhang B, Zhang J, Zhou M, et al. Thermally stable single atom $Pt/m-Al_2O_3$ for selective hydrogenation and CO oxidation. Nat Commun. 2017; 8: 16100.

77. Lu X, Gao S, Lin H, Yu L, Han Y, Zhu P, et al. Bioinspired copper single-atom catalysts for tumor parallel catalytic therapy. Adv Mater. 2020; 32: 2002246.